Investigation of mode-II delamination fracture energy with a discontinuous computational homogenization model

Ke, Lu; van der Meer, Frans

DOI
10.1016/j.compstruc.2024.107327

Publication date
2024

Document Version
Final published version

Published in
Computers and Structures

Computers and Structures 296 (2024) 107327

Contents lists available at ScienceDirect

Computers and Structures

journal homepage: www.elsevier.com/locate/compstruc

Investigation of mode-II delamination fracture energy with a discontinuous computational homogenization model

Lu Ke *, Frans van der Meer

Faculty of Civil Engineering and Geosciences, Delft University of Technology, PO Box 5048, 2600 GA Delft, the Netherlands

ARTICLE INFO

Keywords:
Computational homogenization
Delamination
Fracture energy
Plasticity
Composites

ABSTRACT

Numerical methods for delamination analysis, such as the cohesive zone method, require fracture energy as an essential input. Existing formulations rely on a phenomenological relationship that links fracture energy to the mode of fracture based on linear elastic fracture mechanics (LEFM). However, doubts exist about the applicability of LEFM. It has been demonstrated that the phenomenological relationships describing fracture energy as a function of mode-ratio are not universally valid. Computational homogenization (FE^2) provides an alternative where the dissipative mechanisms can be resolved on the microscale. This paper aims to assess the suitability of a proposed discontinuous FE^2 framework for characterizing delamination growth under mode-II conditions by comparing it to direct numerical simulations (DNS). The impact of plasticity on effective fracture energy is evaluated for two distinct mode-II test configurations. The dissipation density from the bulk integration points within the delamination propagation zone is monitored. The findings demonstrate the FE^2 model's capability to accurately capture plastic energy dissipation around a growing crack. Variations in plastic dissipation are observed between the mTCT and ENF test setups, leading to differences in effective mode-II fracture energy. These nuances, unaccounted for in state-of-the-art mesoscale cohesive models, highlight the FE^2 framework's potential for enhancing delamination modeling.

1. Introduction

Due to the relatively low interlaminar strength, composite laminates are susceptible to delamination. Delamination can lead to significant loss of load-bearing capacity of laminates. Moreover, this failure mode is often visually imperceptible in most practical applications, which requires sophisticated non-destructive detection methods [1,2] to inspect. Thus, during the design phase of laminated composite structures, it is crucial to analyze the extent of potential delamination in order to ensure structural reliability.

In the past decades, extensive research has been conducted to study the delamination, both experimentally and numerically. There exist a number of excellent review articles [3–7] in literature on this topic. For modeling delamination, the dominant approach is based on the cohesive zone method (CZM) that was introduced by Dugdale [8] and Barenblatt [9] in early sixties. The CZM can describe both initiation based on the interfacial strength and crack growth based on the material fracture energy. Ortiz and Pandolfi [10] introduced a 3D cohesive element using irreversible cohesive laws to accurately track dynamic crack growth. Alfano and Crisfield [11] presented a finite element analysis method using interface elements and cohesive laws to assess delamination in laminated composites. Camanho et al. [12] proposed a decohesion interface element with a softening law employing a relative displacement-based damage parameter to simulate delamination under mixed-mode loading. Iannucci [13] presented a CZM-based interface modeling method for explicit FE simulation of dynamic delamination progress in composites. Bouhala et al. [14] proposed a CZM/XFEM-based inverse method for identification of mode-I failure parameters of unidirectional carbon/epoxy composite. Turon et al. [15] proposed a mode-dependent penalty stiffness in the cohesive law to improve the accuracy of delamination simulation using the CZM.

The fracture energy which is an input in these models strongly influences the rate and extent of delamination growth. In order to accurately simulate delamination growth, it is crucial to reliably characterize the fracture energy as a model input. Numerous test methods [4,16] have been proposed to quantify the fracture energy for mode-I, mode-II and mixed-mode I/II delamination fracture, such as the double cantilever beam (DCB) [17] [18], end-notched flexure (ENF) [19,20], end-loaded split (ELS) [21,22], transverse crack tension (TCT) [23,24] and mixed-

* Corresponding author.
E-mail addresses: l.ke@tudelft.nl (L. Ke), f.p.vandermeer@tudelft.nl (F. van der Meer).

https://doi.org/10.1016/j.compstruc.2024.107327
Received 3 October 2023; Accepted 22 February 2024
Available online 1 March 2024

mode bending (MMB) [25–27] tests. With the experimental results at certain given mode ratio, numerical models need to generalize such fracture energy input to deal with the arbitrary changing mode ratio during the simulation. Thus, phenomenological relations on the macroscale are used to characterize the fracture energy as function of mode ratio. The common assumption that fracture energy depends purely on fracture mode-ratio is rarely debated. However, there is evidence that reality is more complex than that. Davidson et al. [28] showed from measurements on a wide range of tests that the measured fracture energy as function of mode ratio does not collapse on a single line. Pérez-Galmés et al. [29] investigated different bending-dominated mode-II test setups for adhesive crack growth and found little difference between the different setups. However, when comparing bending-dominated (ENF) to extension-dominated (TCT) measurements several experimental studies have shown a difference in measured mode-II fracture energy between the two tests [30,31], although Allegri et al. [32] reported similar mode-II fracture energy for both setups. Wisnom [33] reported a size-effect in mode-II fracture energy. Uncertainty about the general applicability of fracture energy measurements endangers the accuracy of state-of-the-art numerical models for progressive failure analysis. Thus, an investigation into the energy dissipation mechanisms in the delamination process that govern the fracture energy is relevant to improve the reliability of macroscale CZM predictions.

Since composite materials are intrinsically heterogeneous, dissipative processes among the constituents are naturally described on the microscale. The major dissipation mechanisms include fiber breakage/bridging, matrix-microcracking/crazing, fiber-matrix debonding and matrix plasticity [34–36]. Computational micromechanical models have been proposed in literature to predict the nonlinear response up to failure of composite materials. Based on the concept of a statistically representative volume element (RVE) [37], deformation and failure of fibers, matrix and fiber/matrix interfaces in the microstructure of composites can be explicitly modeled by relatively simple constitutive laws. Subjected to fundamental loading cases, the micromodel response is then upscaled to the effective response of the composite material via homogenization. For example, by adopting micromechanics-based analysis, several papers [38–41] studied failure envelopes of composite materials by extracting maximum stress values from RVE simulations. McCarthy and Vaughan [42] proposed micromechanics models to extract macroscale elastic moduli and effective strength properties while Naya et al. [43] adopted similar method but include influence from different environmental conditions such as temperature and humidity. Fu and Wang [44] developed a micromechanical model to predict the effective cohesive strengths of all the three delamination modes in unidirectional laminates.

However, in fracture tests, the local strain history that is seen is not as simple as in fundamental loading scenarios such as simple tension or pure shear. The stress or strain path that a macroscale material point near the crack plane follows in a fracture test is not proportional. The nonlinear interaction between neighboring material points in and around the failure process zone (FPZ) makes it impossible to predict the strain path at any point on the macroscale before solving the full problem. Therefore, in order to use a micromodel for describing the material response in a fracture test, a fully coupled approach is needed. This can be achieved either by explicitly modeling the microstructure in (part of) the macroscopic domain with an embedded cell model [45–48] in a direct numerical simulation (DNS), or by coupling an RVE simulation to every macroscopic integration point using computational homogenization (or FE^2) [49]. In the DNS approach, a region with fully-resolved microstructure is modeled around the FPZ while a coarse mesh with homogenized material properties is adopted in the rest of the specimen. Due to the large scale difference between the full problem and the micro-constituents, a highly refined mesh is required to discretize the embedded cell region, which limits the applicability of DNS to a relatively small-scale crack propagation modeling. Moreover, for the typical scenario, where delamination grows in the direction parallel to the fibers, a 2D modeling approach is not suitable while a 3D DNS model is simply not feasible due to the formidable computational cost.

With the FE^2 approach no assumptions on the constitutive response of the homogenized material are needed. The point-wise overall response on the macroscale is directly evaluated, on the fly, from a representative lower scale problem which accounts for the microstructural geometry and properties of the constituents [50]. The strain from the macroscale is translated to microscale boundary conditions, for which the microscale boundary value problem (BVP) is solved after which averaged stresses are passed back to the macromodel. When localization takes place, the classical first-order FE^2 approach [51] becomes problematic because the averaged response becomes pathologically dependent on the size of the micromodel. To overcome the issue of the first-order FE^2 approach, several models have been proposed in recent years. For instance, Massart et al. [52] proposed to use a two-fold first-order FE^2 to resolve the response in both damaging and unloading material parts where an embedded discontinuity band is incorporated at the macroscale while on the microscale localization bands appear as a consequence of softening material laws. Nguyen et al. [53] proposed a continuous-discontinuous FE^2 framework to model the transition of microscopic diffusive damage to macroscopic cohesive failure for tensile cracking problems. Turteltaub and Suárez-Millán [54] established an energetically-consistent FE^2 framework that upscales the microscopic cohesive traction to macroscale discontinuity. Yu [55] proposed a vector-based damage-driven computational homogenization approach with localized gradient enhanced boundary conditions to resolve the RVE size dependency issue. For detailed review, readers are referred to the contributions of [56], [57] and [58]. Most formulations involve a discontinuous formulation on the macroscale, such that the micromodel is used to provide a traction-separation relation. The size of the micromodel can then be included in the scale transition to recover RVE-size independence in the macroscopic response [50].

However, to authors' knowledge the proposed FE^2 approaches for localization problems have not been used beyond the proof-of-principle level. With a view to establish a standard for analyzing the macroscopic effective fracture energy from FE^2 simulations, the applicability of FE^2 approaches for composite delamination has to be proven. To define a case study, mode-II delamination is of particular interest for three reasons. Firstly, there is evidence that the effective fracture energy under pure mode-II depends on the test setup [23,31,33]. Secondly, unlike mode-I dominated cases, longitudinal shear failure has rarely been investigated via microscale simulations. For example, in [59] where mode-II delamination is studied via an analytical homogenization method based on plate theory, the smallest considered scale is still the mesoscale where the composite ply is modeled as a homogeneous material. Lastly, there is significant plastic deformation in mode-II delamination. This has been observed experimentally with digital image correlation by Jalalvand et al. [60]. Furthermore, in a numerical investigation Van der Meer and Sluys [61] showed that plasticity is likely to play a role in the experimental observations by Wisnom [33] on the existence of a size effect in the TCT test.

In this contribution, the suitability of the previously proposed discontinuous FE^2 framework [50] for describing crack growth in an elasto-plastic medium under mode-II conditions is verified by comparison with DNS. The influence of plasticity on the total energy dissipation per unit crack length is assessed for two different tests, namely the ENF and modified TCT [23] setup to exemplify what kind of insight the multiscale approach can provide. Because DNS of an actual fiber reinforced matrix composite for the case where the crack grows in direction parallel to the fibers is not computationally feasible, a simplified layered microstructure is devised with alternating thin layers of elastic and elasto-plastic material and with the possibility of debonding along the interface between the layers. Note that the adopted layered simplified microstructure is not fully representative of actual UD composite. However, it does share essential characteristics in having long straight reinforcements that govern the direction of crack growth combined

with a softer matrix that can undergo plastic deformation. Consistency between FE^2 and DNS results for this case verifies the FE^2 approach for this type of problems. Further analysis of the model results demonstrates how FE^2 analysis can be employed to investigate the source of energy dissipation in material characterization tests. Special attention is given to the question to what extend the multiscale model confirms the observation that effective macroscopic fracture energy depends on the test setup.

2. Modeling strategies

2.1. Failure computational homogenization framework

The two-scale failure computational homogenization framework proposed in Ke and van der Meer [50] is briefly described in this section. Two superscripts, namely $\square^{\mathrm{M}}$ and $\square^{\mathrm{m}}$, are adopted to indicate macroscopic and microscopic quantities, respectively.

2.1.1. Macroscopic problem

The macroscopic problem is schematically shown in Fig. 1. Cohesive cracks are represented by displacement discontinuities along the internal boundary Γ_d^{M} (lines in two-dimensions or surfaces in three-dimensions) within the solid domain Ω^{M}. At the position of the internal boundary, the material splits in two, giving rise to two opposite surfaces ${}^{+}\Gamma_d^{\mathrm{M}}$ and ${}^{-}\Gamma_d^{\mathrm{M}}$. Cohesive tractions $\mathbf{t}_d^{\mathrm{M}} = {}^{-}\mathbf{t}_d^{\mathrm{M}}$ are present across Γ_d^{M} and related to the displacement jump, i.e. $[\![\mathbf{u}^{\mathrm{M}}]\!] = {}^{+}\mathbf{u}^{\mathrm{M}} - {}^{-}\mathbf{u}^{\mathrm{M}}$ where $\mathbf{u}^{\mathrm{M}}$ is the displacement field. The outward unit normal vector is denoted by $\mathbf{n}_d^{\mathrm{M}}$ that points to the positive side ${}^{+}\Gamma_d^{\mathrm{M}}$. Prescribed displacements $\hat{\mathbf{u}}$ are applied on Dirichlet boundary Γ_u^{M} while tractions $\hat{\mathbf{t}}$ are imposed on Neumann boundary Γ_t^{M}.

Exploiting the balance of virtual work and under the small displacement-gradient assumption, the weak form of the equilibrium can be expressed as

$$\int_{\Omega^{\mathrm{M}}\setminus\Gamma_d^{\mathrm{M}}} \nabla^{\mathrm{sym}}\delta\mathbf{u}^{\mathrm{M}} : \boldsymbol{\sigma}^{\mathrm{M}}\mathrm{d}\Omega + \int_{\Gamma_d^{\mathrm{M}}} \delta[\![\mathbf{u}^{\mathrm{M}}]\!]\cdot\mathbf{t}_d^{\mathrm{M}}\mathrm{d}\Gamma = \int_{\Gamma_t^{\mathrm{M}}} \delta\mathbf{u}^{\mathrm{M}}\cdot\hat{\mathbf{t}}\mathrm{d}\Gamma, \tag{1}$$

where the left-hand-side contains the contribution from the bulk material and the cohesive cracks while the right-hand-side is the external virtual work. ∇^{sym} refers to the symmetric gradient. Bulk constitutive laws relate the stress $\boldsymbol{\sigma}^{\mathrm{M}}$ to the bulk strain $\boldsymbol{\varepsilon}^{\mathrm{M}}$ while traction-separation laws relate the cohesive traction $\mathbf{t}_d^{\mathrm{M}}$ and displacement jump $[\![\mathbf{u}^{\mathrm{M}}]\!]$ as well as the bulk strain $\boldsymbol{\varepsilon}^{\mathrm{M}}$, as follows,

$$\boldsymbol{\sigma}^{\mathrm{M}} = \boldsymbol{\sigma}^{\mathrm{M}}(\boldsymbol{\varepsilon}(\mathbf{u}^{\mathrm{M}}),\kappa); \quad \mathbf{t}_d^{\mathrm{M}} = \mathbf{t}_d^{\mathrm{M}}([\![\mathbf{u}^{\mathrm{M}}]\!],\boldsymbol{\varepsilon}(\mathbf{u}^{\mathrm{M}}),\omega), \tag{2}$$

where κ and ω are internal variables. Note that Eq. (2) also includes the dependency of the cohesive traction on the surrounding bulk strain, which is claimed an advantageous cohesive formulation in van der Meer and Sluys [62], and is also present in the current FE^2 framework. Due to the fact that material histories such as plasticity and damage are tracked on the microscale it is not necessary to explicitly define the internal variables on the macroscale.

2.1.2. Kinematics scale transition

The macroscopic deformation measures are defined separately in the continuous part of the domain $\Omega_c^{\mathrm{M}} \overset{\mathrm{def}}{=} \Omega^{\mathrm{M}} \setminus \Gamma_d^{\mathrm{M}}$ and the discontinuous part Γ_d^{M}. For the bulk integration points in the continuous part, the macrostrain field $\boldsymbol{\varepsilon}^{\mathrm{M}}$ is described as

$$\boldsymbol{\varepsilon}_c^{\mathrm{M}} = \nabla^{\mathrm{sym}}\mathbf{u}^{\mathrm{M}} \tag{3}$$

while for the cohesive integration points on Γ_d^{M}, it is defined as

$$\boldsymbol{\varepsilon}_d^{\mathrm{M}} = \boldsymbol{\varepsilon}_b^{\mathrm{M}} + \boldsymbol{\varepsilon}_f^{\mathrm{M}} \tag{4}$$

with

$$\boldsymbol{\varepsilon}_b^{\mathrm{M}} \overset{\mathrm{def}}{=} \frac{1}{2}(\boldsymbol{\varepsilon}^{+}_{\Gamma_d^{\mathrm{M}}} + \boldsymbol{\varepsilon}^{-}_{\Gamma_d^{\mathrm{M}}}) \quad \text{and} \quad \boldsymbol{\varepsilon}_f^{\mathrm{M}} \overset{\mathrm{def}}{=} \frac{1}{h}([\![\mathbf{u}^{\mathrm{M}}]\!] \otimes^{sym} \mathbf{n}_d^{\mathrm{M}}), \tag{5}$$

where $\boldsymbol{\varepsilon}_b^{\mathrm{M}}$ is the bulk strain average from ${}^{+}\Gamma_d^{\mathrm{M}}$ and ${}^{-}\Gamma_d^{\mathrm{M}}$; $\boldsymbol{\varepsilon}_f^{\mathrm{M}}$ is the second-order discontinuity tensor. Note that a scaling parameter h is introduced in the latter quantity. It functions to regulate the energetic equivalence between two scales in order to fulfill the extended Hill-Mandel macrohomogeneity principle [63] and to guarantee RVE-size objectivity in the homogenized response. The value of h is acquired from the underlying microscopic problem accounting for the developed failure mechanism and morphology of the microstructure. Readers are referred to [50] for detailed discussion on the definition of h. In the current work where a microstructure with thin layers of two material (as shown in Fig. 2) is devised for the longitudinal mode-II delamination, the value of h simply equals the height of the RVE.

On the microscale, the displacement field is defined in the first-order FE^2 approach as:

$$\mathbf{u}^{\mathrm{m}} = \mathbf{u}^{\mathrm{M}} + \boldsymbol{\varepsilon}^{\mathrm{M}}\cdot\mathbf{x}^{\mathrm{m}} + \tilde{\mathbf{u}}^{\mathrm{m}}, \tag{6}$$

where $\boldsymbol{\varepsilon}^{\mathrm{M}}$ is either $\boldsymbol{\varepsilon}_c^{\mathrm{M}}$ or $\boldsymbol{\varepsilon}_d^{\mathrm{M}}$; $\tilde{\mathbf{u}}^{\mathrm{m}}$ is the displacement fluctuation field inside the RVE domain; and $\mathbf{x}^{\mathrm{m}}$ is the position vector. The kinematics scale transition is completed by adopting appropriate boundary conditions (BCs) on the RVE to form the microscopic boundary value problem. Different types of BCs exist for microscale problems with localization in literature [see e.g. 64–67]. For the simulation in the present work, node-to-node periodic BCs (as schematically shown in Fig. 3) are adopted.

2.1.3. Stress and traction homogenization

At the converged state of the microscopic BVP, microscale quantities are upscaled to the macroscale via homogenization.

The macroscopic stress at bulk points in Ω_c^{M} is obtained through averaging as

$$\boldsymbol{\sigma}_c^{\mathrm{M}} = \langle\boldsymbol{\sigma}^{\mathrm{m}}\rangle_{\Omega^{\mathrm{m}}} = \frac{1}{|\Omega^{\mathrm{m}}|}\int_{\Omega^{\mathrm{m}}} \boldsymbol{\sigma}^{\mathrm{m}}\mathrm{d}\Omega, \tag{7}$$

where $\langle\square\rangle_{\Omega^{\mathrm{m}}}$ denotes the domain averaging operation; $|\Omega^{\mathrm{m}}|$ is the measure of the domain Ω^{m} which is the area for two-dimensions and volume for three-dimensions.

Combining Eq. (7) with the Cauchy theorem, cohesive tractions for points on the macroscale discontinuity Γ_d^{M} are given as,

$$\mathbf{t}_d^{\mathrm{M}} = \boldsymbol{\sigma}^{\mathrm{M}}\cdot\mathbf{n}_d^{\mathrm{M}}. \tag{8}$$

2.1.4. Macroscopic localization criteria

Localization criteria are crucial for accurate detection of the initiation and propagation of the macroscale cohesive crack. As in [68] and [69], we adopt a bifurcation criterion based on singularity of the acoustic tensor,

$$\begin{aligned} &\text{Find} \quad \mathbf{n}_d^{\mathrm{M}} \Rightarrow \mathbf{Q}\cdot\mathbf{m} = \mathbf{0} \quad \text{at the first time } t_B \text{ for any } \mathbf{m} \\ &\text{with} \quad \mathbf{Q} = \mathbf{n}_d^{\mathrm{M}}\cdot\mathbf{D}^{\mathrm{M}}\cdot\mathbf{n}_d^{\mathrm{M}} \quad \text{and} \quad ||\mathbf{n}_d^{\mathrm{M}}|| = ||\mathbf{m}|| = 1 \end{aligned} \tag{9}$$

where $\mathbf{D}^{\mathrm{M}}$ is the macroscopic bulk tangent stiffness; $\mathbf{Q}$ is the corresponding acoustic tensor; and $\mathbf{m}$ is the polarization vector indicating the initial displacement jump velocity.

A sweeping procedure is used with the parameterization of the normal vector $\mathbf{n}_d^{\mathrm{M}}$ in terms of spherical coordinates. Once the global minimum of $\det(\mathbf{Q})$ turns negative, it is identified that bifurcation occurs at this load step and $\mathbf{m}$ is also computed as the eigenvector of $\mathbf{Q}$ associated with the negative eigenvalue.

In order to robustly discern the correct localization angle regardless of the loading scheme, an extra condition has been proposed in [50] to reinforce the Condition (9). At the load step when $\det(\mathbf{Q})$ turns negative for the first time, if multiple negative local minima are detected, we select that non-positive stationary point of which the failure mode is mostly aligned with the bulk strain field $\boldsymbol{\varepsilon}^{\mathrm{M}}$:

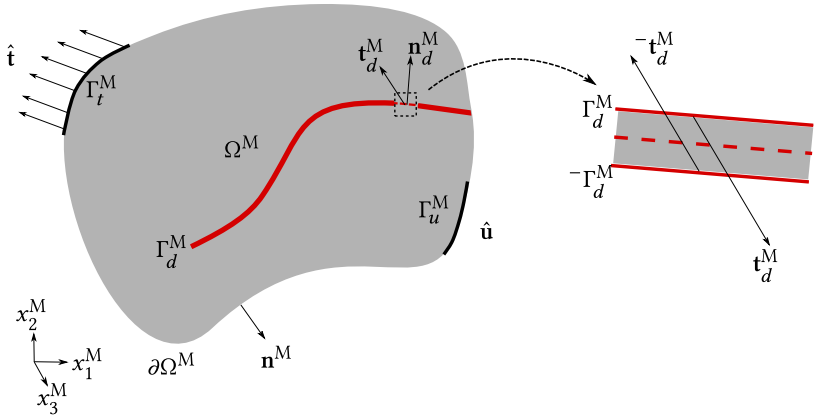

Fig. 1. Cohesive failure problem on macroscale.

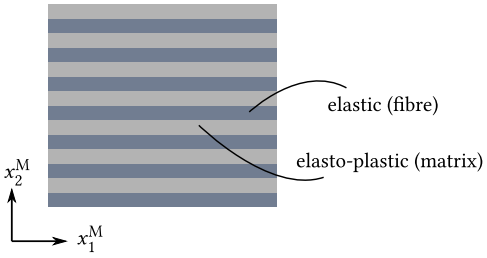

Fig. 2. Simplified microstructure with alternating layers of elastic and elasto-plastic material.

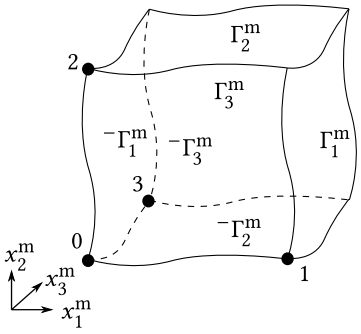

Fig. 3. Node-to-node periodic BCs on 3D RVE, which reads $\mathbf{u}_{+\Gamma_i^{\mathrm{m}}} = \mathbf{u}_{-\Gamma_i^{\mathrm{m}}} + \mathbf{u}_i$ with $i = 1, 2, 3$ and $\mathbf{u}_0 = \mathbf{0}$.

$$\text{Find} \quad (\mathbf{m}, \mathbf{n}_d^{\mathrm{M}}) \Rightarrow \text{Maximum}(\boldsymbol{\varepsilon}^{\mathrm{M}} : (\mathbf{m} \otimes^{sym} \mathbf{n}_d^{\mathrm{M}})). \tag{10}$$

2.2. Implementations

As a natural match with the discrete cohesive fracture problem, the phantom node method [70] is adopted in the present work to model discontinuities on the macroscale. On the microscale as well as in DNS, a model that inserts interelement cohesive elements into the finite element mesh dynamically on the fly is adopted [71,48].

The solution algorithm is a Newton-Raphson iterative procedure with an extra check for cohesive segment insertion at the end of each converged load step. In order to handle the possible snapback behavior, a dissipation-based arclength approach combined with a dynamic switching strategy between load control and dissipation control is adopted [72,73].

2.2.1. Phantom node model

In the phantom node method, cohesive cracks are simulated by duplicating elements in which the localization criteria are violated. A triangular element with original nodes $[n_1, n_2, n_3]$ and one bulk integration point (IP) as schematically shown in Fig. 4 serves as an example. Once the localization is detected, the element domain Ω^{M} is split by a new cohesive segment Γ_d^{M} into subdomains, Ω_A^{M} and Ω_B^{M}, where $\Omega_A^{\mathrm{M}} \bigcup \Omega_B^{\mathrm{M}} = \Omega^{\mathrm{M}}$. Two new elements, A and B, with connectivities being $\text{nodes}_A = [n_1, \tilde{n}_2, \tilde{n}_3]$ and $\text{nodes}_B = [\tilde{n}_1, n_2, n_3]$, now replace the original element. They are partially active within the subdomains Ω_A^{M} and Ω_B^{M}, respectively. The displacement field within Ω^{M} now reads:

$$\mathbf{u}^{\mathrm{M}}(\mathbf{x}^{\mathrm{M}}) = \begin{cases} \mathbf{N}(\mathbf{x}^{\mathrm{M}})\mathbf{u}_A, & \mathbf{x}^{\mathrm{M}} \in \Omega_A^{\mathrm{M}} \\ \mathbf{N}(\mathbf{x}^{\mathrm{M}})\mathbf{u}_B, & \mathbf{x}^{\mathrm{M}} \in \Omega_B^{\mathrm{M}} \end{cases}, \tag{11}$$

where $\mathbf{N}(\mathbf{x}^{\mathrm{M}})$ is the standard shape function matrix. The displacement jump along Γ_d^{M} is defined as:

$$[\![\mathbf{u}(\mathbf{x}^{\mathrm{M}})]\!]^{\mathrm{M}} = \mathbf{N}(\mathbf{x}^{\mathrm{M}})\left(\mathbf{u}_A - \mathbf{u}_B\right), \quad \mathbf{x}^{\mathrm{M}} \in \Gamma_d^{\mathrm{M}}. \tag{12}$$

Following Eq. (5), the bulk macrostrain along the discontinuity is evaluated in Voigt notation as

$$\boldsymbol{\varepsilon}_b^{\mathrm{M}} = \frac{1}{2}\mathbf{B}(\mathbf{u}_A + \mathbf{u}_B) \tag{13}$$

where $\mathbf{B}$ is the strain-displacement matrix which is the same for both overlapping elements, while the smeared discontinuity strain is defined as

$$\boldsymbol{\varepsilon}_f^{\mathrm{M}} = \frac{1}{h}\mathbf{A}\mathbf{N}\left(\mathbf{u}_A - \mathbf{u}_B\right), \quad \text{where} \quad \mathbf{A}^T = \begin{bmatrix} n_{d1}^{\mathrm{M}} & 0 & n_{d2}^{\mathrm{M}} \\ 0 & n_{d2}^{\mathrm{M}} & n_{d1}^{\mathrm{M}} \end{bmatrix}. \tag{14}$$

For partially-active elements A and B and the cohesive crack segment, new integration schemes need to be constructed. To determine integration weights, triangulation is performed for the bulk elements. When the constant strain triangular element is used, only one bulk RVE is present in the uncracked element, which is cloned to all newly allocated bulk and cohesive IPs, with the deformation state at the localization. When multiple IPs are used for macro-elements, a cloning operation is performed based on the distance between old and new IPs such that the new RVE is copied from the closest old IP.

It is worth mentioning that the secant unloading stiffness can be used as an alternative for the new bulk IPs if linear unloading is assumed, as discussed in [53]. This strategy is beneficial for the computational robustness since unloading could sometimes incur convergence issues in the microscopic simulations. Note that the secant unloading stiffness does include the effect of material damage that has accumulated before the element is cracked.

2.2.2. Interelement cohesive model

For the microscopic problem in the FE^2 simulation and DNS cases, a model [71] that inserts cohesive elements between neighboring elements during the simulation is adopted in order to reduce computa-

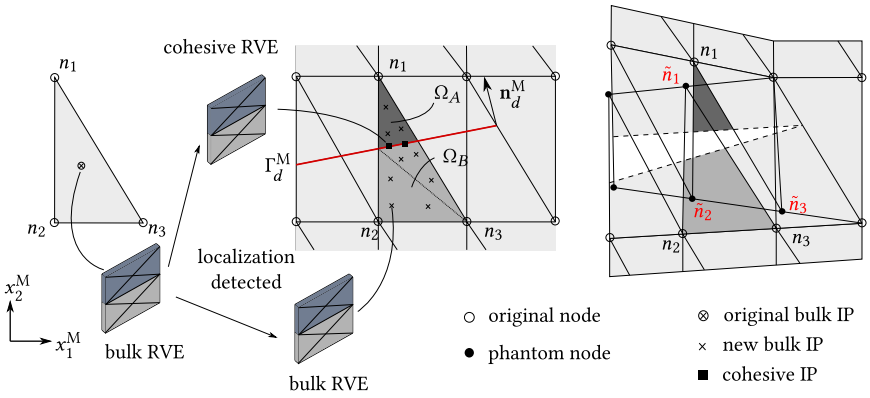

Fig. 4. Phantom node model with cohesive segments on the macroscale while 3D slice RVEs are adopted on the microscale.

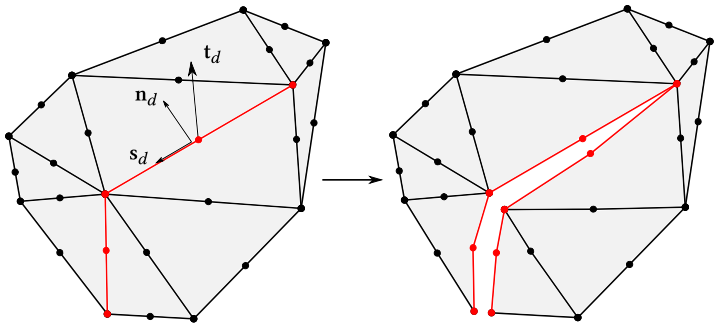

Fig. 5. Insertion of interelement cohesive element.

tional costs and achieve good robustness, which is especially important for DNS cases.

Second-order six-node triangular elements are adopted to discretize the specimen domain in 2D problems. For 3D microscopic models in the current FE^2 simulation, the 2D mesh is extruded to a 3D mesh with only one element in the thickness direction (the longitudinal direction on the macroscale). As a result, six-node triangular elements are extended to twelve-node wedge elements.

Cohesive cracks can only initiate at the mid-node and propagate along element edges (see Fig. 5) when the following local failure criterion is violated,

$$\bar{\sigma} \geq f_t \quad \text{with} \quad \bar{\sigma} = \begin{cases} \sqrt{\left(t_n\right)^2 + \beta\left(|t_s|\right)^2}, & [\![u]\!]_n \geq 0 \\ \sqrt{\beta}\left(|t_s| - \mu\, |t_n|\right), & [\![u]\!]_n < 0 \end{cases}, \tag{15}$$

where $\bar{\sigma}$ is the effective stress, f_t is the material tensile strength, t_n and t_s is the normal and shear traction component, β is a shear stress factor and μ is the friction coefficient. In 3D, t_s is the norm of the two shear components. At every converged load step this criterion is checked at every mid-node in the mesh. Because the crack insertion introduces unbalance force the Newton-Raphson procedure is re-performed until equilibrium is reached again.

Because the cohesive element is inserted at a non-zero stress state, it is necessary to adopt an initially rigid cohesive law [72]. To achieve this without introducing a singularity at zero-opening, we shift the origin of a non-rigid cohesive law (bilinear) such that the traction at zero displacement jump and zero damage matches the surrounding bulk stress on the mid-node from the bulk element, as shown in Fig. 6 (see [48] for more details).

2.2.3. Plasticity model

For the elasto-plastic 'matrix' material, the pressure dependent hardening plasticity model developed by Melro et al. [41] for polymers is adopted. The model is briefly described in the following.

The stress is related to the strain via

$$\boldsymbol{\sigma} = \mathbf{D}_{\mathrm{e}} : (\boldsymbol{\varepsilon} - \boldsymbol{\varepsilon}_{\mathrm{p}}) \quad \text{with} \quad D_{ijkl} = G\left(\delta_{ij}\delta_{kl} + \delta_{il}\delta_{jk}\right) + \left(K - \frac{2}{3}G\right)\delta_{ij}\delta_{kl} \tag{16}$$

where $\mathbf{D}_{\mathrm{e}}$ is the elastic stiffness tensor, $\boldsymbol{\varepsilon}_p$ is the plastic strain, K is the bulk modulus and G is the shear modulus.

A paraboloidal yield function is defined as:

$$f\left(\boldsymbol{\sigma}, \sigma_{\mathrm{c}}, \sigma_{\mathrm{t}}\right) = 6J_2 + 2I_1\left(\sigma_{\mathrm{c}} - \sigma_{\mathrm{t}}\right) - 2\sigma_{\mathrm{c}}\sigma_{\mathrm{t}} \tag{17}$$

where J_2 is the second deviatoric stress invariant and I_1 is the first invariant. The compression yield stress σ_{c} and tension yield stress σ_{t} are not constant but rather a function of the equivalent plastic strain $\varepsilon_{\mathrm{p}}^{eq}$, which is defined as

$$\dot{\varepsilon}_{\mathrm{p}}^{\mathrm{eq}} = \sqrt{k\dot{\boldsymbol{\varepsilon}}_{\mathrm{p}} : \dot{\boldsymbol{\varepsilon}}_{\mathrm{p}}} \quad \text{with} \quad k = 1/(1 + 2\nu_p) \tag{18}$$

where ν_p is the plastic Poisson ratio, introduced by Guild et al. [74] and also adopted by Melro et al. [75].

A non-associative flow rule is introduced to describe the increment in plastic strain as:

$$\Delta\boldsymbol{\varepsilon}_{\mathrm{p}} = \Delta\gamma\left(3\mathbf{S} + \frac{1 - 2\nu_{\mathrm{p}}}{1 + \nu_{\mathrm{p}}} I_1 \mathbf{I}\right) \tag{19}$$

where $\Delta\gamma$ is the increment of plastic multiplier and $\mathbf{S}$ is the deviatoric stress tensor.

In the current implementation, the plastic dissipation density d^{M} is monitored for analyzing the plastic contribution in the energy dissipation along the delamination growth, defined as:

$$d^{\mathrm{M}} = \int_0^t \boldsymbol{\sigma} : \dot{\boldsymbol{\varepsilon}}_{\mathrm{p}} dt. \tag{20}$$

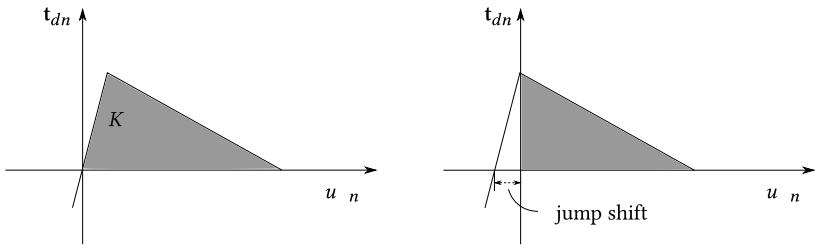

(a) Initially stiff cohesive law (b) Shifted cohesive law

Fig. 6. Pure mode I representation of shift in cohesive law to mimic initially rigid behavior.

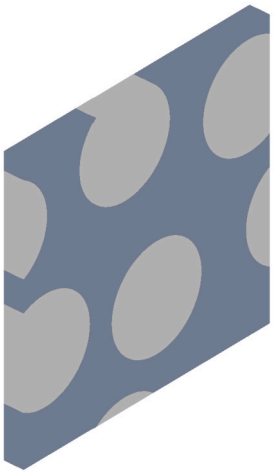

Fig. 7. 3D RVE for unidirectional fiber-reinforced composite material.

Note that in the FE^2 simulation, the plastic dissipation density is an average over the RVE volume.

2.2.4. 3D slice RVE

As the concerned longitudinal mode-II delamination can be simulated accurately in 2D, the FE^2 implementation as well as the DNS is applied to a plane strain macroscopic problem. However, when considering a microstructure of fiber-reinforced composite material a 3D micromodel is needed, because the plane in which the microstructural geometry can be described (the transverse plane) is perpendicular to the plane in which the macroscopic geometry and boundary conditions can be described. Thus, for the simplified microstructure shown in Fig. 2, we also use a 3D RVE. Under the assumption that fibers are straight and perfectly aligned, a 3D RVE can be obtained by extruding a 2D RVE to a single element in fiber direction, as the one in Fig. 7. Such slice RVE is able to capture the interaction between longitudinal shear and stress in fiber direction [35]. Notably, the slice itself does not describe crack growth in longitudinal direction. However, in line with the concept of separation of scales, a series of slice RVEs representing different stages of material degradation can be representative for the FPZ of a growing crack.

3. Test setup and material properties

Two mode-II delamination tests, ENF and modified TCT specimen, are chosen to investigate the suitability of the failure FE^2 framework with a slice RVE for simulating shear crack growth in unidirectional laminates. The setups of both tests are schematically given in Fig. 8. In both specimens, a notch (shown in red lines) is pre-defined ahead of a critical region (shown in blue) over which the microstructure is modeled, either with FE^2 or with the embedded DNS model. In the modified TCT specimen (or mTCT), as proposed by Scalici et al. [23], horizontal pre-cracks are included, extending from both ends of the vertical notch to create a pre-crack in the form of a lying H, which makes the test more well-behaved as compared to the classical TCT test with only the vertical notch. Due to the symmetric test setup with symmetric response, only one quarter of the mTCT specimen is modeled to reduce the computational cost without affecting the numerical results, following several earlier studies in literature where the (modified) TCT setup has been modeled numerically [61,23,76,77].

For the elasto-plastic 'matrix' material, the plasticity model is used with the hardening curve adapted from Fiedler et al. [78], as shown in Fig. 9. Note that moderate hardening tails are added to both compression and tension curves for compatibility with the stress-based cohesive initiation criterion. The Poisson's ratio in the matrix is $\nu_m = 0.3$ and Young's modulus is $E_m = 10\,100$ MPa, while the plastic Poisson's ratio $\nu_{mp} = 0.39$ [35]. The 'fibers' are modeled as isotropic linear elastic with Poisson's ratio $\nu_f = 0.2$ and Young's modulus $E_f = 121\,000$ MPa. 'Fiber/matrix' debonding is modeled with the shifted cohesive law described in Section 2.2.2.

Interfacial parameters are given in Table 1. The initial stiffness is decided by preliminary simulations. It is chosen as high as possible without endangering the computational convergence. The fracture energy is chosen in the range of measured mode-II values of composites with epoxy matrix reported in literature [79,80]. It is assumed to already include the effect of increased crack surface due to formation of cusps or hackles [81]. The chosen value for β is combined with the chosen value for f_t to ensure that shear failure happens just before the maximum value of the matrix shear stress-strain curve. The relative value of the strength with respect to plasticity hardening curve has a strong influence on the contribution of plasticity to the energy dissipation. Further increase of the strength would lead to pure matrix plastic deformation without interface cracking. Because only mode-II cases are considered in this paper, similar results could be obtained with a lower β in combination with a lower value for f_t. Finally, a low μ limits the effect from compressive normal traction which is anyway very small in the mode-II case.

The micromodel contains a number of parameters, some of which are standard and independently identifiable, like the elastic properties of the matrix and fiber, while others may be more difficult to identify, such as the plastic Poisson's ratio for the matrix and the fiber/matrix interfacial properties. In line with the motivation for FE^2, it is assumed in this work that a micromodel with realistic parameters exist and that the present micromodel includes the relevant physical ingredients.

4. Results and discussion

In mode-II delamination crack growth, there is a thin layer of material around the crack in which crack growth is accompanied by significant plastic deformations. In a homogenized model, and therefore also on the macroscale in FE^2 model, a sufficiently refined mesh is needed to capture this accurately [61]. Furthermore, the FE^2 model relies on the principle of separation of scales, meaning that every macroscopic integration point represents a region with uniform deformation apart from a microscopic fluctuation that can be modeled as periodic. The principle of separation of scales requires that the microstructural length scale, in

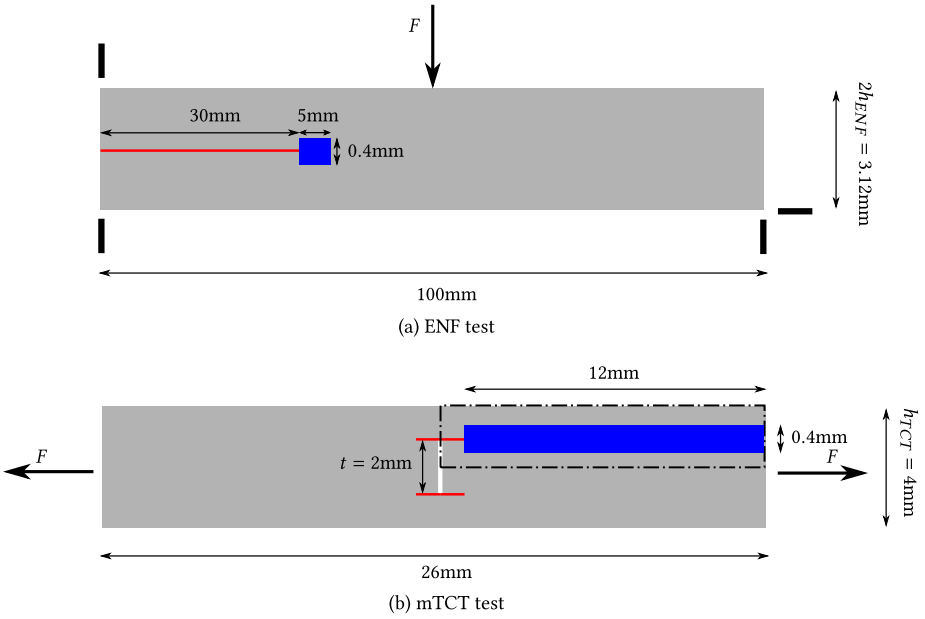

Fig. 8. ENF and mTCT tests setups. (For clarity, figures not to scale.)

Table 1
Material parameters of cohesive laws.

Penalty stiffness K_p (N/mm^3)	Fracture strength f_t (MPa)	Fracture energy G_c (N/mm)	Interaction coefficient β	Friction coefficient μ
1.0e5	60	1.5	0.8	0.1

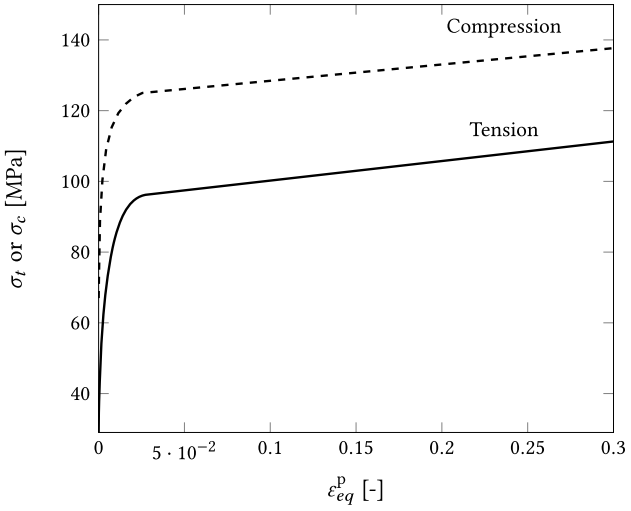

Fig. 9. Hardening curves for the plasticity model.

this case the thickness of the layers, is small with respect to the length scale of macroscopic variations, in this case the thickness of the plastic zone around the crack. In light of these considerations, agreement between DNS and FE^2 requires sufficiently thin layers in the DNS and a sufficiently refined mesh in the FE^2. Therefore, a twofold convergence study is performed on these two aspects. The results are compared in terms of global load-displacement response and predicted plastic energy dissipation.

4.1. Mesh refinement study

The discretization in the critical region where delamination cracks propagate is illustrated in Fig. 10. Six-node triangle elements are adopted for DNS cases while for FE^2 cases four-node quadrilateral elements are used. For the mesh refinement study, we progressively reduce the thickness of individual layers (t_{DNS}) in the DNS mesh and thickness of element layers (t_{FE^2}) in the FE^2 mesh. Table 2 shows the considered varying thickness values. Note that due to the much thinner plastic layer in ENF tests than in mTCT tests, t_{FE^2} of the ENF mesh is set to smaller values than those of the mTCT mesh.

Table 2
Thickness of material layers in DNS and macro-element in FE^2.

Case	t_{DNS} (μm)	t_{FE^2} (μm)
ENF	5, 4, 3.125, 2.5	14.8,10.8,8.9,6.6
mTCT	5, 4, 3, 2.5	80, 57.1, 44.4

4.1.1. ENF test

The load-displacement curves at the loading point of ENF simulations are shown in Fig. 11. A load drop can be observed following the peak point due to the propagation of the delamination crack. Although the curves start to increase again soon because of the short region where crack growth is allowed, a region with stable crack growth is achieved. The position of the load drop is governed by the effective fracture energy consisting of a cohesive and a plastic contribution.

From the convergence study in Fig. 11, it is observed that the FE^2 results have converged. For the DNS, a slight mesh-dependence remains for the investigated layer thicknesses. Further refinement is challenging, because the finest mesh simulations are already heavy and convergence of the nonlinear solution procedure deteriorated for finer meshes. Nevertheless, the DNS results are close to the converged FE^2 solution and the finest DNS solution is considered representative for more detailed comparison with the FE^2 solution.

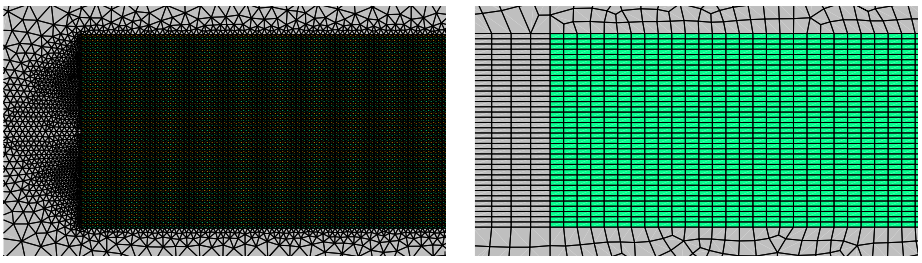

(a) (b)

Fig. 10. Mesh in critical region. (a) DNS case; (b) FE^2 case.

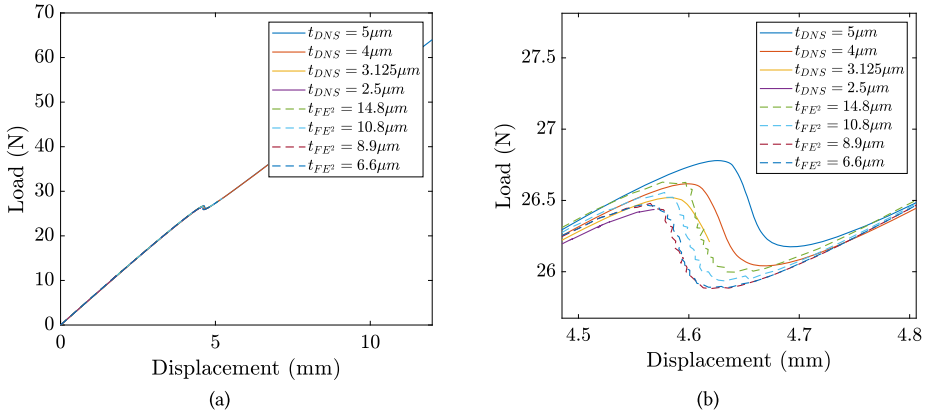

(a) (b)

Fig. 11. Load-displacement responses at the loading point of ENF tests. (a) global view; (b) zoom-in around the peak.

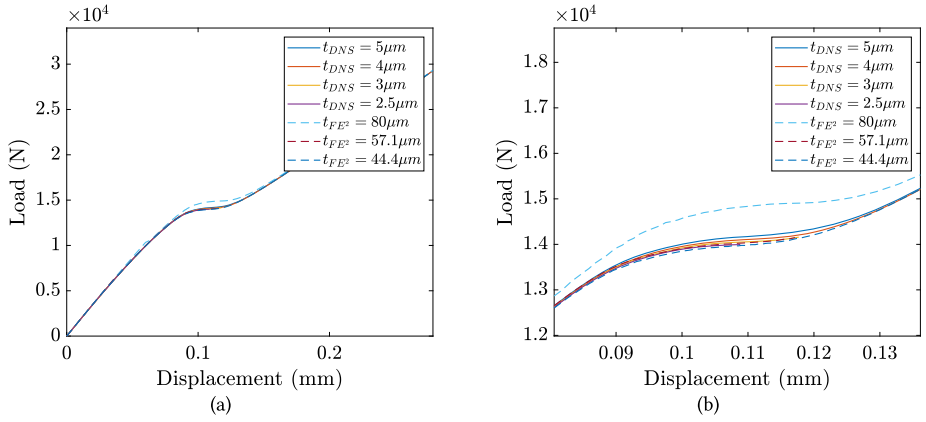

(a) (b)

Fig. 12. Load-displacement responses at the loading point of mTCT tests. (a) global view; (b) zoom-in around the plateau.

4.1.2. *mTCT test*

For the mTCT simulations, load-displacement curves are shown in Fig. 12. A plateau is present in the curve indicating the stable propagation of delamination. Even more than in the ENF test, both DNS and FE^2 results converge to a very close unique response. This means that the FE^2 model in this case yields highly accurate solution compared to the DNS model. It is also clear that a relatively coarse macromesh in the FE^2 model is already good enough to capture the plastic zone around the delamination crack. This will be clarified via the plastic energy dissipation analysis in next section.

4.2. *Plastic dissipation along crack propagation*

To quantify the plastic contribution to the fracture energy i.e. the energy dissipation per unit crack growth, the dissipation density of a column of bulk integration points is integrated over the height of the critical region. The dissipation is firstly analyzed for an individual cross-section over the height of the specimen after which the longitudinal variation of the integrated quantity is examined. The results from the finest-mesh simulations are adopted except where mesh size is explicitly mentioned.

4.2.1. *ENF test*

Fig. 13 shows the dissipation density from ENF simulations at each integration point over the height of the cross-section at $x = 32$ mm. The results are from the final time step in the analysis when the delamination crack has propagated well beyond the cross section under consideration. The results of the DNS ($t_{DNS} = 3.125$ µm) in Fig. 13 (a) show a staggered pattern due to the fact that dissipation only occurs in the elasto-plastic 'matrix' layer. By contrast, for the FE^2 cases, the macroscopic values are obtained by averaging over the two layers in the RVE. Thus, for comparison purposes, the DNS results are also averaged. It is clear that a significant amount of plastic deformation is

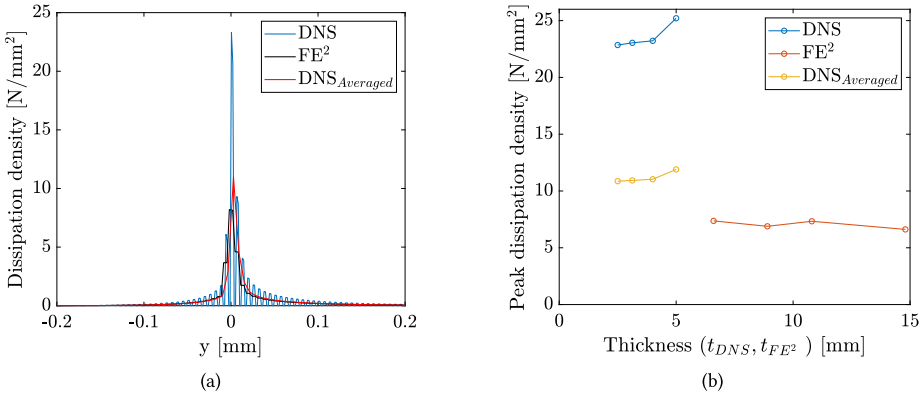

Fig. 13. Dissipation density over the cross-section at location $x = 32$ mm in ENF test. (a) results from the case $t_{DNS} = 3.125$ µm; (b) convergence of the peak value of the dissipation density profile.

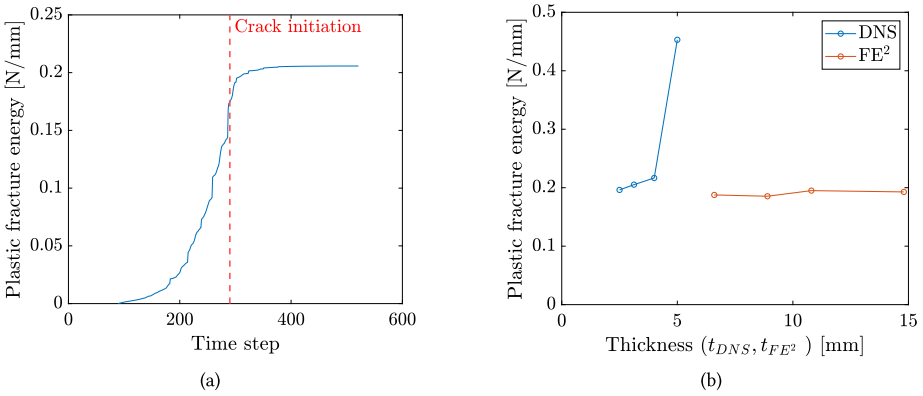

Fig. 14. (a) Evolution of plastic fracture energy at $x = 32$ mm in ENF test from the DNS case with $t_{DNS} = 3.125$ µm; (b) convergence of the plastic fracture energy at $x = 32$ mm.

present in the central layers adjacent to the crack plane. DNS results show a higher plastic concentration than the FE^2 results. This could explain the small difference which exists in Fig. 11. Fig. 13 (b) shows the peak of the dissipation density profiles at different layer thicknesses. The values are the average of the peaks from $x = 31.9$ mm $\sim$ 32.1 mm for each data point in order to mitigate any spurious fluctuations. The peak exhibits a converged trend with a decreasing layer thickness in DNS cases while in FE^2 cases it oscillates with a very small variance. However, the difference between the DNS and FE^2 peaks is not negligible even after averaging over two DNS layers.

After integrating the density over the height of the cross-section, the plastic contribution to the fracture energy at a certain x-location can be obtained. Fig. 14 (a) shows the evolution of such a value at $x = 32$ mm corresponding to the DNS case with $t_{DNS} = 3.125$ µm. It can be observed that the time window over which plastic energy is dissipated in this cross section is relatively narrow. Plastic dissipation starts when the fracture process zone approaches the considered location and stops soon after decohesion starts at this x-location. Hence, from macroscopic perspective, all plastic energy dissipation contributes to the fracture energy. We call the cumulative plastic dissipation under unit crack length the *plastic fracture energy*. Fig. 14 (b) shows the convergence of the final integrated plastic fracture energy at $x = 32$ mm with regard to difference layer thicknesses. It is observed that FE^2 simulations yield a result that is almost identical to the converged DNS result. Again, the plotted values are the averages from $x = 31.9$ mm $\sim$ 32.1 mm for each data point in order to mitigate any spurious fluctuations.

Fig. 15 shows the plastic fracture energy profile along the crack path at different time steps. At the top the progression of cohesive crack segments is visualized, with the blue line indicating the initial cohesive crack, and the red line indicating the traction free crack. Plastic deformation initiates just ahead of the crack tip and further develops as the crack approaches. When crack cohesive initiation takes place, plastic dissipation stops, which leads to a plateau in the profile curve. A similar pattern can be found in the FE^2 results, as shown in Fig. 16 except at the location of the initial crack tip ($x = 30$ mm). At this point the phantom node mesh with a sharp crack tip on an element edge is apparently not sufficiently refined to capture the stress field accurately, while the principle of separation of scales is also violated with the sharp crack tip. Another difference between FE^2 and DNS is observed in more noticeable oscillations in the FE^2 solution. A finer macromesh or more cohesive integration points might be needed to get a smoother solution. Comparing the final profiles from DNS and FE^2 models, a good agreement in the amount of plastic dissipation around the growing crack is observed.

4.2.2. mTCT test

For the mTCT test, the same analysis is carried out. Fig. 17 shows the dissipation density at each integration point over the height of cross-section at $x = 5$ mm. Same as for the ENF test, averaging is done for the DNS case. However, unlike with the ENF test, Fig. 17 shows an excellent agreement between the DNS and FE^2 results not only in the shape but also in terms of the exact values obtained. The FE^2 model in this case predicts the plastic dissipation in the critical region very accurately. It is worth noting that the plastic region in the mTCT test is much wider than that in the ENF test. This makes the mTCT models converge faster to the unique solution.

Regarding the plastic fracture energy profile along the crack path, Fig. 18 and Fig. 19 show the evolution for the DNS case and the FE^2 case, respectively. Very similar plastic dissipation in terms of the shape and maximum value is obtained with the two models. Small oscillations

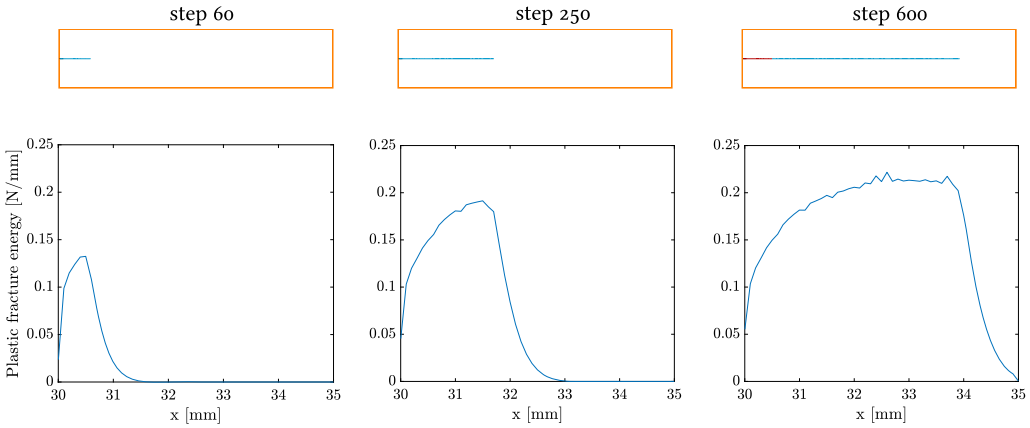

Fig. 15. Plastic fracture energy along the whole crack path from DNS model in ENF test.

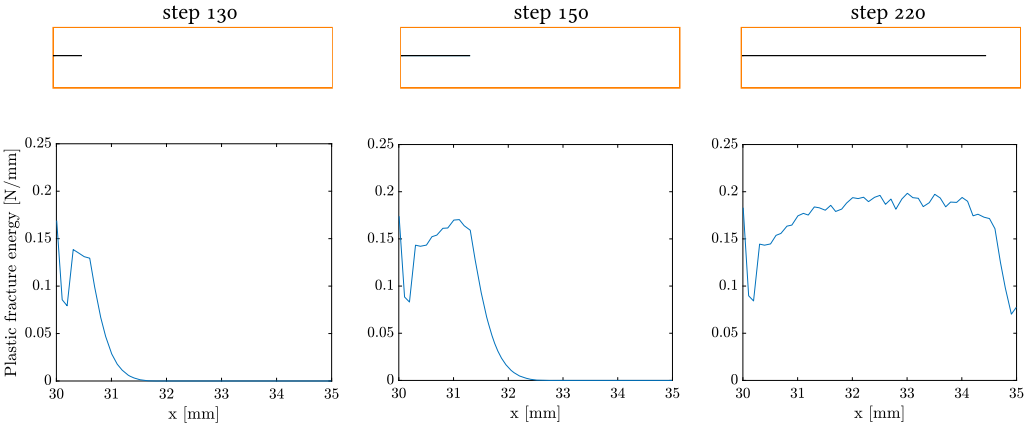

Fig. 16. Plastic fracture energy along the whole crack path from FE^2 model in ENF test.

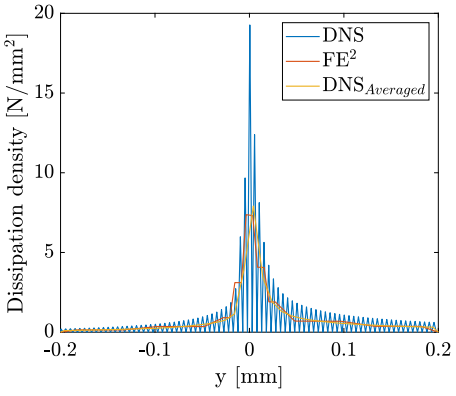

Fig. 17. Dissipation density over the cross-section at location $x = 5$ mm in mTCT test.

are visible in both results but these are expected to vanish with a more refined mesh. As for the ENF test, the FE^2 model accurately represents the local dissipation processes observed in the DNS reference solution.

4.2.3. ENF test vs. mTCT test

Comparing the maximum plastic fracture energy in from the two test cases, it appears that the mTCT test has a significantly higher contribution from the plastic deformation which further leads to a higher total fracture energy G_c. The total fracture energy can also be assessed by the theoretical solution or comparison to simulations with elastic bulk behavior, collapsing all nonlinear behavior in a cohesive crack.

Due to the relatively large FPZ, the existing analytical solutions for the ENF test such as the definition given by [82] do not yield very accurate results if directly compared to the numerical load-displacement curve. Thus, we run the test with elastic matrix material and vary the cohesive fracture energy to test which effective value of the fracture energy gives a good match with the simulations that include plasticity. This is equivalent to performing a macroscale simulation with elastic bulk and effective fracture energy. The results are compared to the previous FE^2 result in Fig. 20. First we set the cohesive fracture energy to 1.5 N/mm, which is the same as was used for the cohesive cracks in the simulations with plasticity. It is observed that the global response deviates significantly from the simulation that did include plasticity, which confirms that the plastic dissipation increases the effective fracture energy. Then the cohesive fracture energy is set to 1.68 N/mm, adding the plastic fracture energy which was found to be around 0.18 N/mm. Now, the load-displacement curve is very close to that from the FE^2 simulation that includes plasticity, although a small difference is found around the peak load. In order to further confirm the equivalence of the fracture energy, we analyze the total dissipated energy when traction-free crack tip reached $x = 31.0$ mm (near the lowest point of the softening branch in Fig. 20) for both cases. For the plastic case, it is 4.55 J while it is 4.48 J for the elastic case with $G_c^{\text{elastic}} = 1.68$ N/mm. Two values are close, which validates the prediction of the total dissipation of the FE^2 approach.

For the mTCT test, fracture energy can be computed analytically as

$$G^T = \frac{\sigma^2 h_{TCT} t}{4E_1(h_{TCT} - t)} \tag{21}$$

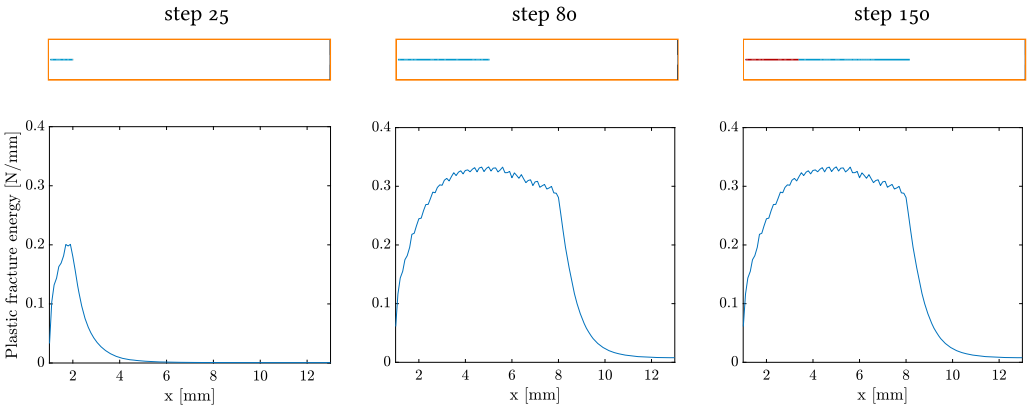

Fig. 18. Plastic fracture energy along the whole crack path from DNS model in mTCT test.

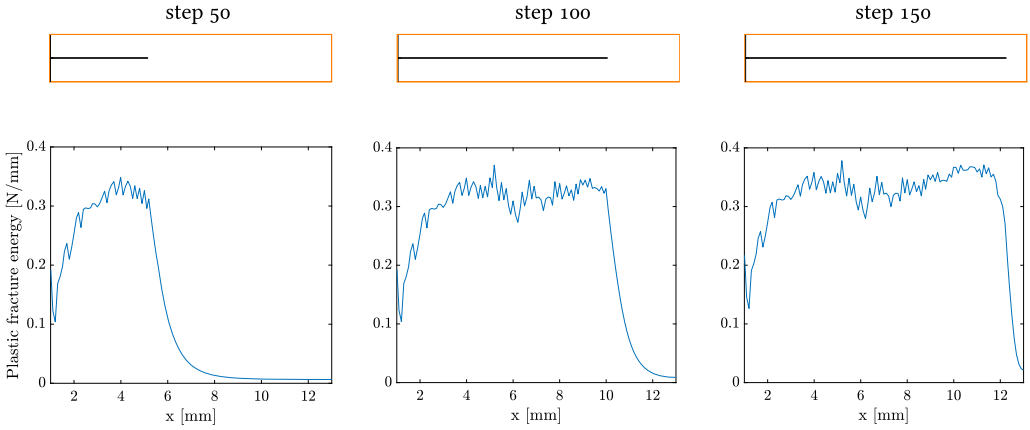

Fig. 19. Plastic fracture energy along the whole crack path from FE^2 model in mTCT test.

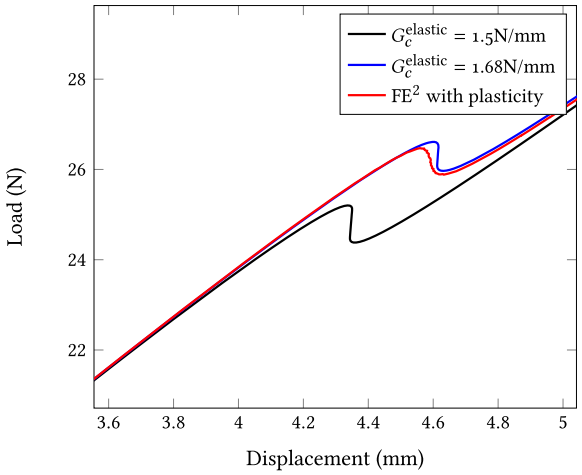

Fig. 20. Load-displacement response from ENF simulations, comparing the FE^2 simulations to simulations with homogenized elastic bulk behavior and as interfacial fracture energy of 1.5 N/mm and 1.68 N/mm.

where σ is the propagation stress corresponding to the plateau in the load-displacement curve and t the thickness of the cut plies. By adopting the load when traction-free crack initiates in Fig. 12, we can obtain $G^T_{c_{DNS}} = 1.84\,\text{N/mm}$ and $G^T_{c_{FE^2}} = 1.83\,\text{N/mm}$. This indicates that $G_{plastic} \approx 0.33\,\text{N/mm}$ which is in the range of the results in Fig. 19.

Comparing the reference solutions of the ENF and mTCT test, it is shown that the latter has a higher effective fracture energy. An equivalent cohesive law with fracture energy that includes a plastic contribution exists for both tests separately, but the effective G_c depends on the test setup and can therefore not be considered a material property.

5. Conclusion

A multiscale framework for modeling mode-II delamination in unidirectional composites has been developed. In this paper, it is shown through comparison with DNS on a material with simplified microstructure that the FE^2 model can capture plastic energy dissipation around a growing crack accurately. The multiscale model response is independent from the RVE size as shown in earlier work [50], and here it is also shown that the model response is independent on the macroscale element size. However, a very fine mesh is needed on the macroscale in order to obtain an objective response, especially for the ENF test where the plastic zone around the delamination crack is particularly narrow. In order to assess the plastic contribution to the total fracture energy, we propose to explicitly monitor the dissipation density from the bulk integration points in the zone where the delamination propagates. Dissipation is integrated over the height to obtain the plastic fracture energy. It is found that there is a high concentration of plastic dissipation right next to the crack, with a zone of gradually decreasing plastic dissipation in the surrounding layers. This concentration, shown as the peak in the dissipation profile, is not converged between DNS and FE^2 with the adopted layer thicknesses. However, the integrated plastic fracture energy converges much faster for both types of tests. In a comparison between two mode-II setups, it is observed that the material experiences more plastic dissipation in the mTCT test than in the ENF test. Due to the difference in plastic dissipation, the mode-II fracture energy does not exist as a material property for the investigated system. To investigate to what extend that also is the case for actual

fiber-reinforced composites, larger RVEs with realistic microstructure and material parameters need to be adopted. The requirement of using highly refined meshes on the macroscale to properly resolve the plastic zone around the growing crack makes multiscale simulations with realistic microstructure excessively expensive. This exacerbates the need for acceleration techniques [83,84] to speed up microscale simulations.

Funding

This work was supported by the Dutch Research Council NWO [grant number 16464].

CRediT authorship contribution statement

Lu Ke: Writing – original draft, Validation, Software, Methodology, Investigation, Conceptualization. **Frans van der Meer:** Writing – review & editing, Supervision, Resources, Project administration, Funding acquisition.

Declaration of competing interest

The authors declare that they have no known competing financial interests or personal relationships that could have appeared to influence the work reported in this paper.

Data availability

Data will be made available on request.

References

[1] Lim Dao Kun, Mustapha KB, Pagwiwoko CP. Delamination detection in composite plates using random forests. Compos Struct 2021;278:114676. https://doi.org/10.1016/j.compstruct.2021.114676. ISSN 02638223. Available from: https://linkinghub.elsevier.com/retrieve/pii/S0263822321011338.

[2] Zhang Zhifang, Shankar Krishna, Morozov Evgeny V, Tahtali Murat. Vibration-based delamination detection in composite beams through frequency changes. J Vib Control 2014;22(2):496–512. https://doi.org/10.1177/1077546314533584.

[3] Elder David J, Thomson Rodney S, Nguyen Minh Q, Scott Murray L. Review of delamination predictive methods for low speed impact of composite laminates. Compos Struct 2004;66(1–4):677–83. https://doi.org/10.1016/j.compstruct.2004.06.004.

[4] Brunner AJ, Blackman BRK, Davies P. A status report on delamination resistance testing of polymer–matrix composites. Eng Fract Mech 2008;75(9):2779–94. https://doi.org/10.1016/j.engfracmech.2007.03.012.

[5] Tabiei Ala, Zhang Wenlong. Composite laminate delamination simulation and experiment: a review of recent development. Appl Mech Rev 2018;70(3). https://doi.org/10.1115/1.4040448. Available from: https://asmedigitalcollection.asme.org/appliedmechanicsreviews/article/doi/10.1115/1.4040448/367470/Composite-Laminate-Delamination-Simulation-and.

[6] Tay TE. Characterization and analysis of delamination fracture in composites: an overview of developments from 1990 to 2001. Appl Mech Rev 2003;56(1):1–32. https://doi.org/10.1115/1.1504848. Available from: https://asmedigitalcollection.asme.org/appliedmechanicsreviews/article/56/1/1/463637/Characterization-and-analysis-of-delamination.

[7] Wang Wandong, Teixeira De Freitas Sofia, Poulis Johannes A, Zarouchas Dimitrios. A review of experimental and theoretical fracture characterization of bi-material bonded joints. Composites, Part B, Eng 2021;206:108537. https://doi.org/10.1016/j.compositesb.2020.108537. Available from: http://creativecommons.org/licenses/by/4.0/.

[8] Dugdale DS. Yielding of steel sheets containing slits. J Mech Phys Solids 1960;8(2):100–4. https://doi.org/10.1016/0022-5096(60)90013-2.

[9] Barenblatt GI. The mathematical theory of equilibrium cracks in brittle fracture. Advances in applied mechanics, vol. 7. Elsevier; 1962. p. 55–129. Available from: https://linkinghub.elsevier.com/retrieve/pii/S0065215608701212.

[10] Ortiz M, Pandolfi A. Finite-deformation irreversible cohesive elements for three-dimensional crack-propagation analysis. Int J Numer Methods Eng 1999;44(9):1267–82. https://doi.org/10.1002/(SICI)1097-0207(19990330)44:9<1267::AID-NME486>3.0.CO;2-7. Available from: http://doi.wiley.com/10.1002/(SICI)1097-0207(19990330)44:9<1267::AID-NME486>3.0.CO;2-7. https://onlinelibrary.wiley.com/doi/10.1002/(SICI)1097-0207(19990330)44:9%3C1267::AID-NME486%3E3.0.CO;2-7.

[11] Alfano G, Crisfield MA. Finite element interface models for the delamination analysis of laminated composites: mechanical and computational issues. Int J Numer Methods Eng 2001;50(7):1701–36. https://doi.org/10.1002/nme.93. Available from: http://doi.wiley.com/10.1002/nme.93.

[12] Camanho PP, Davila CG, de Moura MF. Numerical simulation of mixed-mode progressive delamination in composite materials. J Compos Mater 2003;37(16):1415–38. https://doi.org/10.1177/0021998303034505. Available from: http://journals.sagepub.com/doi/10.1177/0021998303034505.

[13] Iannucci L. Dynamic delamination modelling using interface elements. Comput Struct 2006;84:1029. https://doi.org/10.1016/J.COMPSTRUC.2006.02.002.

[14] Bouhala Lyazid, Makradi Ahmed, Belouettar Salim, Younes Anis, Natarajan Sundararajan. An XFEM/CZM based inverse method for identification of composite failure parameters. Comput Struct 2015;153:91. https://doi.org/10.1016/J.COMPSTRUC.2015.02.035.

[15] Turon A, González EV, Sarrado C, Guillamet G, Maimí P. Accurate simulation of delamination under mixed-mode loading using a cohesive model with a mode-dependent penalty stiffness. Compos Struct 2018;184:506–11. https://doi.org/10.1016/j.compstruct.2017.10.017. ISSN 02638223.

[16] Davies P, Blackman BRK, Brunner AJ. Standard test methods for delamination resistance of composite materials: current status. Appl Compos Mater 1998;5:6. https://doi.org/10.1023/A:1008869811626. Available from: https://link.springer.com/article/10.1023/A:1008869811626.

[17] Wagner W, Balzani C. Simulation of delamination in stringer stiffened fiber-reinforced composite shells. Comput Struct 2008;86:930. https://doi.org/10.1016/J.COMPSTRUC.2007.04.018.

[18] ASTM. Standard test method for mode I interlaminar fracture toughness of unidirectional fiber-reinforced polymer matrix composites; 2013.

[19] de Moura Marcelo FSF, Silva Manuel AL, Morais José JL, de Morais Alfredo B, Lousada José JL. Data reduction scheme for measuring G IIc of wood in end-notched flexure (ENF) tests. Holzforschung 2009;63(1):99–106. https://doi.org/10.1515/HF.2009.022. Available from: https://www.degruyter.com/document/doi/10.1515/HF.2009.022/html.

[20] Gliszczynski A, Wiącek N. Experimental and numerical benchmark study of mode II interlaminar fracture toughness of unidirectional GFRP laminates under shear loading using the end-notched flexure (ENF) test. Compos Struct 2021;258:113190. https://doi.org/10.1016/j.compstruct.2020.113190. ISSN 02638223.

[21] Blackman BRK, Brunner AJ, Williams JG. Mode II fracture testing of composites: a new look at an old problem. Eng Fract Mech 2006;73(16):2443–55. https://doi.org/10.1016/j.engfracmech.2006.05.022. ISSN 00137944. Available from: https://linkinghub.elsevier.com/retrieve/pii/S0013794406002086.

[22] Pérez-Galmés M, Renart J, Sarrado C, Rodríguez-Bellido A, Costa J. A data reduction method based on the J-integral to obtain the interlaminar fracture toughness in a mode II end-loaded split (ELS) test. Composites, Part A, Appl Sci Manuf 2016;90:670–7. https://doi.org/10.1016/j.compositesa.2016.08.020. ISSN 1359835X. Available from: https://linkinghub.elsevier.com/retrieve/pii/S1359835X16302767.

[23] Scalici T, Pitarresi G, Catalanotti G, van der Meer FP, Valenza A. The Transverse Crack Tension test revisited: an experimental and numerical study. Compos Struct 2016;158:144–59. https://doi.org/10.1016/j.compstruct.2016.09.033. ISSN 02638223. Available from: https://www.sciencedirect.com/science/article/pii/S0263822316306134.

[24] Hahn Philipp, Channammagari Harichandana, Imbert Mathieu, May Michael. High-rate mode II fracture toughness testing of polymer matrix composites using the Transverse Crack Tension (TCT) test. Composites, Part B, Eng 2022;233:109636. https://doi.org/10.1016/j.compositesb.2022.109636. ISSN 13598368. Available from: https://linkinghub.elsevier.com/retrieve/pii/S1359836822000245.

[25] Kinloch AJ, Wang Y, Williams JG, Yayla P. The mixed-mode delamination of fibre composite materials. Compos Sci Technol 1993. https://doi.org/10.1016/0266-3538(93)90031-B.

[26] Benzeggagh ML, Kenane M. Measurement of mixed-mode delamination fracture toughness of unidirectional glass/epoxy composites with mixed-mode bending apparatus. Compos Sci Technol 1996;56(4):439–49. https://doi.org/10.1016/0266-3538(96)00005-X. ISSN 0266-3538. Available from: https://www.sciencedirect.com/science/article/pii/026635389600005X?via%3Dihub.

[27] Sadeghi MZ, Zimmermann J, Gabener A, Schroeder KU. The applicability of J-integral approach in the determination of mixed-mode fracture energy in a ductile adhesive. Int J Adhes Adhes 2018;83:2–8. https://doi.org/10.1016/j.ijadhadh.2018.02.027. ISSN 01437496. Available from: https://linkinghub.elsevier.com/retrieve/pii/S0143749618300666.

[28] Davidson Barry D, Gharibian Simon J, Yu Lijie. Evaluation of energy release rate-based approaches for predicting delamination growth in laminated composites. Int J Fract 2000;105(4):343–65. https://doi.org/10.1023/A:1007647226760. ISSN 03769429.

[29] Pérez-Galmés M, Renart J, Sarrado C, Brunner AJ, Rodríguez-Bellido A. Towards a consensus on mode II adhesive fracture testing: experimental study. Theor Appl Fract Mech 2018;98:210–9. https://doi.org/10.1016/j.tafmec.2018.09.014. ISSN 01678442.

[30] König M, Krüger R, Kussmaul K, Von Alberti M, Gädke M. Characterizing static and fatigue interlaminar fracture behavior of a first generation graphite/epoxy composite. ASTM Spec Tech Publ 1997;1242:60–81.

[31] Fink A, Camanho PP, Andrés JM, Pfeiffer E, Obst A. Hybrid CFRP/titanium bolted joints: performance assessment and application to a spacecraft payload adaptor. Compos Sci Technol 2010;70(2):305–17. https://doi.org/10.1016/j.compscitech.2009.11.002. Available from: https://www.sciencedirect.com/science/article/pii/S0266353809003868.
[32] Allegri G, Jones MI, Wisnom MR, Hallett SR. A new semi-empirical model for stress ratio effect on mode II fatigue delamination growth. Composites, Part A, Appl Sci Manuf 2011;42(7):733–40. https://doi.org/10.1016/J.COMPOSITESA.2011.02.013.
[33] Wisnom MR. On the increase in fracture energy with thickness in delamination of unidirectional glass fibre-epoxy with cut central plies. J Reinf Plast Compos 1992;11:897–909.
[34] Yang Lei, Yan Ying, Liu Yujia, Ran Zhiguo. Microscopic failure mechanisms of fiber-reinforced polymer composites under transverse tension and compression. Compos Sci Technol 2012;72(15):1818–25. https://doi.org/10.1016/j.compscitech.2012.08.001. ISSN 02663538. Available from: https://linkinghub.elsevier.com/retrieve/pii/S0266353812002928.
[35] van der Meer Frans P. Micromechanical validation of a mesomodel for plasticity in composites. Eur J Mech A, Solids 2016;60:58–69. https://doi.org/10.1016/j.euromechsol.2016.06.008. ISSN 09977538.
[36] Danzi F, Fanteria D, Panettieri E, Palermo M. A numerical micro-mechanical study of the influence of fiber–matrix interphase failure on carbon/epoxy material properties. Compos Struct 2017;159:625–35. https://doi.org/10.1016/j.compstruct.2016.09.095. ISSN 02638223. Available from: https://linkinghub.elsevier.com/retrieve/pii/S026382231631409X.
[37] Gitman IM, Askes H, Sluys LJ. Representative volume: existence and size determination. Eng Fract Mech 2007;74(16):2518–34. https://doi.org/10.1016/j.engfracmech.2006.12.021. ISSN 00137944.
[38] Oguni K, Ravichandran G. A micromechanical failure model for unidirectional fiber reinforced composites. Int J Solids Struct 2001;38(40–41):7215–33. https://doi.org/10.1016/S0020-7683(00)00284-5. ISSN 00207683. Available from: https://linkinghub.elsevier.com/retrieve/pii/S0020768300002845.
[39] Totry Essam, González Carlos, LLorca Javier. Failure locus of fiber-reinforced composites under transverse compression and out-of-plane shear. Compos Sci Technol 2008;68(3–4):829–39. https://doi.org/10.1016/j.compscitech.2007.08.023. ISSN 02663538. Available from: https://linkinghub.elsevier.com/retrieve/pii/S0266353807003387.
[40] Romanowicz Marek. A numerical approach for predicting the failure locus of fiber reinforced composites under combined transverse compression and axial tension. Comput Mater Sci 2012;51(1):7–12. https://doi.org/10.1016/j.commatsci.2011.07.039. ISSN 09270256. Available from: https://linkinghub.elsevier.com/retrieve/pii/S0927025611004319.
[41] Melro AR, Camanho PP, Andrade Pires FM, Pinho ST. Micromechanical analysis of polymer composites reinforced by unidirectional fibres: part II-micromechanical analyses. Int J Solids Struct 2013;50(11–12):1906–15. https://doi.org/10.1016/j.ijsolstr.2013.02.007. ISSN 00207683.
[42] McCarthy C, Vaughan T. Micromechanical failure analysis of advanced composite materials. In: Numerical modelling of failure in advanced composite materials; 2015. p. 379–409. Available from: https://www.sciencedirect.com/science/article/pii/B978008100329000141#f0040.
[43] Naya F, González C, Lopes CS, Van der Veen S, Pons F. Computational micromechanics of the transverse and shear behavior of unidirectional fiber reinforced polymers including environmental effects. Composites, Part A, Appl Sci Manuf 2017;92:146–57. https://doi.org/10.1016/j.compositesa.2016.06.018. ISSN 1359835X. Available from: https://linkinghub.elsevier.com/retrieve/pii/S1359835X1630197X.
[44] Fu Chen, Wang Xi. Prediction of the cohesive strength for simulating composite delamination by a micro-mechanical model based on random RVE. Compos Struct 2021;262:113343. https://doi.org/10.1016/j.compstruct.2020.113343.
[45] González Carlos, LLorca Javier. Virtual fracture testing of composites: a computational micromechanics approach. Eng Fract Mech 2007;74(7):1126–38. https://doi.org/10.1016/j.engfracmech.2006.12.013. ISSN 00137944. Available from: https://linkinghub.elsevier.com/retrieve/pii/S0013794406004681.
[46] Arteiro A, Catalanotti G, Melro AR, Linde P, Camanho PP. Micro-mechanical analysis of the in situ effect in polymer composite laminates. Compos Struct 2014;116(1):827–40. https://doi.org/10.1016/j.compstruct.2014.06.014.
[47] Herráez M, González C, Lopes CS. A numerical framework to analyze fracture in composite materials: from R-curves to homogenized softening laws. Int J Solids Struct 2018;134:216–28. https://doi.org/10.1016/j.ijsolstr.2017.10.031. ISSN 00207683.
[48] Liu Y, van der Meer FP, Sluys LJ, Ke L. Modeling of dynamic mode I crack growth in glass fiber-reinforced polymer composites: fracture energy and failure mechanism. Eng Fract Mech 2021;243:107522. https://doi.org/10.1016/j.engfracmech.2020.107522. ISSN 00137944. Available from: https://linkinghub.elsevier.com/retrieve/pii/S0013794420310742.
[49] Feyel Frédéric, Chaboche Jean Louis. FE^2 multiscale approach for modelling the elastoviscoplastic behaviour of long fibre SiC/Ti composite materials. Comput Methods Appl Mech Eng 2000;183(3–4):309–30. https://doi.org/10.1016/S0045-7825(99)00224-8. ISSN 00457825.
[50] Ke Lu, van der Meer Frans P. A computational homogenization framework with enhanced localization criterion for macroscopic cohesive failure in heterogeneous materials. J Theor Comput Appl Mech 2022. https://doi.org/10.46298/jtcam.7707. Available from: https://jtcam.episciences.org/9194.
[51] Kouznetsova VG, Brekelmans WAM, Baaijens FPT. An approach to micro-macro modeling of heterogeneous materials. Comput Mech 2001;27(1):37–48. https://doi.org/10.1007/s004660000212.
[52] Massart TJ, Peerlings RHJ, Geers MGD. An enhanced multi-scale approach for masonry wall computations with localization of damage. Int J Numer Methods Eng 2007;69(5):1022–59. https://doi.org/10.1002/nme.1799. ISSN 00295981. Available from: http://doi.wiley.com/10.1002/nme.1799.
[53] Nguyen Vinh Phu, Stroeven Martijn, Sluys Lambertus Johannes. An enhanced continuous–discontinuous multiscale method for modeling mode-I cohesive failure in random heterogeneous quasi-brittle materials. Eng Fract Mech 2012;79:78–102. https://doi.org/10.1016/j.engfracmech.2011.10.005. ISSN 00137944. Available from: https://www.sciencedirect.com/science/article/pii/S0013794411003845. https://linkinghub.elsevier.com/retrieve/pii/S0013794411003845.
[54] Turteltaub Sergio, Suárez-Millán Rubén. Energetically-consistent multiscale analysis of fracture in composites materials. Eur J Mech A, Solids 2020;84:104079. https://doi.org/10.1016/j.euromechsol.2020.104079. ISSN 09977538. Available from: https://linkinghub.elsevier.com/retrieve/pii/S0997753820304678.
[55] Yu Chenjie. Vector-based damage-driven computational homogenization with localized gradient enhanced boundary conditions for multi-scale modelling of quasi-brittle materials. Comput Struct 2023;280:106985. https://doi.org/10.1016/J.COMPSTRUC.2023.106985.
[56] Phu Nguyen Vinh, Stroeven Martijn, Sluys Lambertus Johannes. Multiscale continuous and discontinuous modeling of heterogeneous materials: a review on recent developments. J Multiscale Model 2011;03(04):229–70. https://doi.org/10.1142/S1756973711000509. Available from: http://www.worldscientific.com/doi/abs/10.1142/S1756973711000509.
[57] Matouš Karel, Geers Marc GD, Kouznetsova Varvara G, Gillman Andrew. A review of predictive nonlinear theories for multiscale modeling of heterogeneous materials. J Comput Phys 2017;330:192–220. https://doi.org/10.1016/j.jcp.2016.10.070. Available from: https://www.sciencedirect.com/science/article/pii/S0021999116305782?via%3Dihub#se0080.
[58] Budarapu Pattabhi Ramaiah, Zhuang Xiaoying, Rabczuk Timon, Bordas Stephane PA. Multiscale modeling of material failure: theory and computational methods. Advances in applied mechanics, vol. 52. Elsevier. ISBN 9780128174791, 2019. p. 1–103. Available from: https://www.sciencedirect.com/science/article/pii/S006521561930002X. https://linkinghub.elsevier.com/retrieve/pii/S006521561930002X.
[59] Massabò Roberta, Darban Hossein. Mode-II dominant fracture of layered composite beams and wide-plates: a homogenized structural approach. Eng Fract Mech 2019;213:280. https://doi.org/10.1016/J.ENGFRACMECH.2019.03.002.
[60] Jalalvand Meisam, Czél Gergely, Fuller Jonathan D, Wisnom Michael R, Canal Luis P, González Carlos D, et al. Energy dissipation during delamination in composite materials – an experimental assessment of the cohesive law and the stress-strain field ahead of a crack tip. Compos Sci Technol 2016;134:115–24. https://doi.org/10.1016/J.COMPSCITECH.2016.08.001. Available from: https://www.sciencedirect.com/science/article/pii/S0266353816308648.
[61] van der Meer Frans P, Sluys LJ. A numerical investigation into the size effect in the transverse crack tension test for mode-II delamination. Composites, Part A, Appl Sci Manuf 2013;54:145–52. https://doi.org/10.1016/j.compositesa.2013.07.013. Available from: https://www.sciencedirect.com/science/article/pii/S1359835X13001978.
[62] van der Meer Frans P, Sluys LJ. A phantom node formulation with mixed mode cohesive law for splitting in laminates. Int J Fract 2009;158(2):107–24. https://doi.org/10.1007/s10704-009-9344-5. Available from: http://link.springer.com/10.1007/s10704-009-9344-5.
[63] Turteltaub Sergio, van Hoorn Niels, Westbroek Wim, Hirsch Christian. Multiscale analysis of mixed-mode fracture and effective traction-separation relations for composite materials. J Mech Phys Solids 2018;117:88–109. https://doi.org/10.1016/j.jmps.2018.04.009. Available from: https://www.sciencedirect.com/science/article/pii/S0022509617306828?via%3Dihub.
[64] Larsson F, Runesson K, Saroukhani S, Vafadari R. Computational homogenization based on a weak format of micro-periodicity for RVE-problems. Comput Methods Appl Mech Eng 2011;200(1–4):11–26. https://doi.org/10.1016/j.cma.2010.06.023. ISSN 00457825.
[65] Coenen EWC, Kouznetsova VG, Geers MGD. Novel boundary conditions for strain localization analyses in microstructural volume elements. Int J Numer Methods Eng 2012;90(1):1–21. https://doi.org/10.1002/nme.3298. ISSN 00295981. Available from: http://doi.wiley.com/10.1002/nme.3298.
[66] Linder Christian, Raina Arun. A strong discontinuity approach on multiple levels to model solids at failure. Comput Methods Appl Mech Eng 2013;253:558–83. https://doi.org/10.1016/j.cma.2012.07.005. Available from: https://www.sciencedirect.com/science/article/pii/S0045782512002253.
[67] Hofman P, Ke L, van der Meer F. Circular microstructural volume elements with periodic boundary conditions for localization problems. In: VIII conference on mechanical response of composites; 2021.
[68] Mercatoris BCN, Bouillard Ph, Massart TJ. Multi-scale detection of failure in planar masonry thin shells using computational homogenisation. Eng Fract Mech 2009;76(4):479–99. https://doi.org/10.1016/J.ENGFRACMECH.2008.10.003.

[69] Oliver J, Caicedo M, Roubin E, Huespe AE, Hernández JA. Continuum approach to computational multiscale modeling of propagating fracture. Comput Methods Appl Mech Eng 2015;294:384–427. https://doi.org/10.1016/j.cma.2015.05.012. Available from: https://www.sciencedirect.com/science/article/pii/S0045782515001851.

[70] Song Jeong-Hoon, Areias Pedro MA, Belytschko Ted. A method for dynamic crack and shear band propagation with phantom nodes. Int J Numer Methods Eng 2006;67(6):868–93. https://doi.org/10.1002/nme.1652. Available from: http://doi.wiley.com/10.1002/nme.1652.

[71] Camacho GT, Ortiz M. Computational modelling of impact damage in brittle materials. Int J Solids Struct 1996;33(20–22):2899–938. https://doi.org/10.1016/0020-7683(95)00255-3. Available from: https://www.sciencedirect.com/science/article/pii/0020768395002553.

[72] van der Meer Frans P. Mesolevel modeling of failure in composite laminates: constitutive, kinematic and algorithmic aspects. Arch Comput Methods Eng 2012;19(3):381–425. https://doi.org/10.1007/s11831-012-9076-y. ISSN 11343060.

[73] Verhoosel Clemens V, Remmers Joris JC, Gutiérrez Miguel A. A dissipation-based arc-length method for robust simulation of brittle and ductile failure. Int J Numer Methods Eng 2009;77(9):1290–321. https://doi.org/10.1002/nme.2447. ISSN 00295981. Available from: http://doi.wiley.com/10.1002/nme.2447.

[74] Guild FJ, Potter KD, Heinrich J, Adams RD, Winsom MR. Understanding and control of adhesive crack propagation in bonded joints between carbon fibre composite adherends II. Finite element analysis. Int J Adhes Adhes 2001;21:445–53. https://doi.org/10.1016/S0143-7496(01)00021-5.

[75] Melro AR, Camanho PP, Andrade Pires FM, Pinho ST. Micromechanical analysis of polymer composites reinforced by unidirectional fibres: part I-constitutive modelling. Int J Solids Struct 2013;50:1897. https://doi.org/10.1016/j.ijsolstr.2013.02.009. ISSN 00207683.

[76] Catalanotti G, Furtado C, Scalici T, Pitarresi G, van der Meer FP, Camanho PP. The effect of through-thickness compressive stress on mode II interlaminar fracture toughness. Compos Struct 2017;182:153–63. https://doi.org/10.1016/J.COMPSTRUCT.2017.09.014. Available from: https://www.sciencedirect.com/science/article/pii/S0263822317318512. Novel TCT experiment of mode II delamination fracture toughness. Could be a reference for the new model validation.

[77] Varandas LF, Arteiro A, Bessa MA, Melro AR, Catalanotti G. The effect of through-thickness compressive stress on mode II interlaminar crack propagation: a computational micromechanics approach. Compos Struct 2017;182:326–34. https://doi.org/10.1016/J.COMPSTRUCT.2017.09.020.

[78] Fiedler B, Hojo M, Ochiai S, Schulte K, Ochi M. Finite-element modeling of initial matrix failure in CFRP under static transverse tensile load. Compos Sci Technol 2001;61(1):95–105. https://doi.org/10.1016/S0266-3538(00)00198-6.

[79] Turon A, Camanho PP, Costa J, Renart J. Accurate simulation of delamination growth under mixed-mode loading using cohesive elements: definition of interlaminar strengths and elastic stiffness. Compos Struct 2010;92(8):1857–64. https://doi.org/10.1016/j.compstruct.2010.01.012. Available from: https://www.sciencedirect.com/science/article/pii/S026382231000022X.

[80] Bonhomme J, Argüelles A, Viña J, Viña I. Fractography and failure mechanisms in static mode I and mode II delamination testing of unidirectional carbon reinforced composites. Polym Test 2009;28(6):612–7. https://doi.org/10.1016/J.POLYMERTESTING.2009.05.003. ISSN 01429418.

[81] O'Brien TK. Composite interlaminar shear fracture toughness, G(IIc) - Shear measurement or sheer myth? In: Bucinell RB, editor. Composite materials: fatigue and fracture, seventh volume; 1998. p. 3–18.

[82] Carlsson LA, Gillespie JW, Pipes RB. On the analysis and design of the end notched flexure (ENF) specimen for mode II testing. J Compos Mater 1986;20(6):594–604. https://doi.org/10.1177/002199838602000606. Available from: http://journals.sagepub.com/doi/10.1177/002199838602000606.

[83] Maia MA, Rocha IBCM, Kerfriden P, van der Meer FP. Physically recurrent neural networks for path-dependent heterogeneous materials: embedding constitutive models in a data-driven surrogate. Comput Methods Appl Mech Eng 2023;407:115934. https://doi.org/10.1016/J.CMA.2023.115934. arXiv:2209.07320.

[84] Rocha IBCM, Kerfriden P, van der Meer FP. On-the-fly construction of surrogate constitutive models for concurrent multiscale mechanical analysis through probabilistic machine learning. J Comput Phys, X 2021;9. https://doi.org/10.1016/J.JCPX.2020.100083. ISSN 25900552.